



# Structure of carbon nanotubes probed by local and global probes

Ph. Lambin<sup>a,\*</sup>, A. Loiseau<sup>b</sup>, C. Culot<sup>a</sup>, L.P. Biró<sup>c</sup>

<sup>a</sup>*Départements de physique et chimie, Facultés Universitaires Notre-Dame de la Paix, 61 Rue de Bruxelles, B 5000 Namur, Belgium*

<sup>b</sup>*Laboratoire d'Etude des Microstructures, UMR No. 104 ONERA-CNRS, Onera, B.P. 72, 92322 Châtillon Cedex, France*

<sup>c</sup>*Research Institute for Technical Physics and Materials Science, P.O. Box 49, H-1525 Budapest, Hungary*

Received 6 March 2001; accepted 12 December 2001

---

## Abstract

A review is proposed of different techniques available today for the characterization of the atomic structure of carbon nanotubes. This review covers the electron microscopies, various diffraction techniques, scanning probe microscopies, and optical spectroscopies, including Raman scattering. The advantages and limitations of the characterization techniques are discussed. © 2002 Published by Elsevier Science Ltd.

*Keywords:* A. Carbon nanotubes; C. Electron microscopy; Raman spectroscopy; Scanning tunneling microscopy; X-ray diffraction

---

## 1. Introduction

The remarkable structure of carbon nanotubes confers them with special properties that most likely will lead to interesting applications [1]. In the case of single-wall nanotubes (SWNT), some of these properties are directly influenced by the way the graphene sheet is wrapped around. This is the case for the electronic structure [2,3] of the nanotube and related properties such as electric transport [4], optical activity [5], and to some extent the mechanical properties [6]. It is obviously clear, then, that a full characterization of the atomic structure of the nanotubes is required to understand the measured properties. This characterization involves the determination of both the diameter and the chiral angle (or helicity which we used as a synonym) of the nanotube, to which the two wrapping indices identifying the SWNT are related. Scanning tunneling microscopy combined with tunneling spectroscopy is the best tool available for that determination (see Section 4).

SWNTs are generally arranged in ropes, and these ropes need to be characterized too. It is now well-established that the nanotubes in a rope can have different helicities and their diameters also can vary within some limits. If, with a

transmission electron microscope or a scanning probe microscope, it is possible to examine the individual tubes in a rope, it might prove advantageous to obtain more global information on the rope constituents. Electron diffraction is particularly well suited for that purpose (see Section 3). At a larger scale, the ropes themselves form entangled networks for which averaged structural data are needed. These can be obtained by X-ray or neutron diffraction (see Section 3), and by Raman scattering (see Section 5).

Multiwall nanotubes (MWNT) certainly will be useful in many applications. Here too, there is a need for structural characterization. This is a complicated task to achieve, because there are many parameters to determine: number of layers, distributions of diameters and chiralities. Yet, MWNTs contain structural defects on which very little is known at the present time [7].

Structural characterization of the nanotubes is also essential to understand the growth mechanisms, to study the influence of the synthesis conditions on the nanotube produced, or to analyze the efficiency of a purification process. In addition to the structural characterization of pure nanotubes, several techniques are used routinely to study the effects of tube doping, core filling, surface coating, gas adsorption etc. These aspects will not be reviewed here. This paper is about the atomic structure of pure nanotubes, how it can be determined with local and global probes, and what are the advantages and limitations

---

\*Corresponding author. Tel.: +32-81-724-710; fax: +32-81-724-707.

E-mail address: [philippe.lambin@fundp.ac.be](mailto:philippe.lambin@fundp.ac.be) (P. Lambin).

of the techniques available today. These techniques have been classified according to four main categories: electron microscopies, diffraction, scanning probe microscopies, and optical spectroscopies including Raman scattering.

## 2. Electronic microscopies

It is by high resolution transmission electron microscopy (HRTEM) combined with electron diffraction that the carbon nanotubes were discovered and their helical structures were elucidated [8]. HRTEM images are phase contrast images of the nanotube atomic structure projected in the observation plane perpendicular to the direction of propagation of the electron beam [9]. Different kinds of information can be extracted from these images: (i) nature of the self organization of the tubes and number of tubes, (ii) diameters of the tubes, (iii) atomic configuration (helicity) of the tubes. The first two characteristics can be easily and routinely determined whereas imaging of the atomic configuration requires very high resolution machines and finely controlled observation conditions.

### 2.1. Organization and diameter of the tubes

Nanotubes are assembled either as Russian dolls (multiwall tubes) (Fig. 1a) or as crystalline ropes of single layer tubes (Fig. 2a). As shown in Fig. 1, multiwall nanotubes are usually observed perpendicularly to their axis. Under these conditions, they are imaged by two sets of parallel and periodic fringes which are due to the part of the coaxial layers parallel to the electron beam (Fig. 1). These portions of the layers, drawn in grey in Fig. 1a, are periodically stacked as the honeycomb (0002) planes of a crystal of graphite oriented in a prismatic orientation. The fringes are therefore equivalent to (0002) lattice fringes of graphite. Image simulations have been performed with the EMS software package [10] in order to determine how their contrast varies with the operating conditions (defocus of the objective lens in particular) and with the thickness of the sample along the direction of propagation of the electron beam. Depending on these parameters, the dark fringes may be located on the atomic planes or in between [11]. The first condition is usually achieved under standard defocus conditions close to so-called Scherzer focus and provides a direct determination of the number of coaxial layers, the inner and outer diameters of the multiwall nanotube. If the layers are perfectly coaxial and cylindrical, the image remains unchanged through a rotation of the multiwall tube around its axis. If this is not the case, the appearance of the fringes can be perturbed in different ways which have been studied in detail in Refs. [12–14]. For instance, if the multiwall tube has a polygonal cross section, the part of the layers which are parallel to the beam are not necessarily the (0002) planes of graphite and may correspond to another family of graphite planes: the

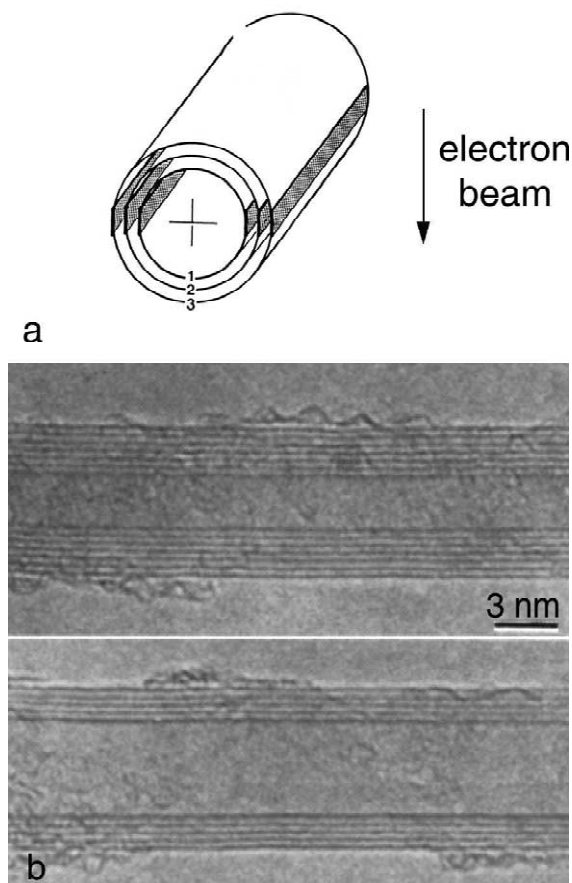


Fig. 1. High resolution TEM analysis of a multiwall nanotube. (a) Scheme of the conditions of observation. The nanotube is projected along the direction of propagation of the electron beam indicated by the arrow. The contrast observed on the image is issued from the portions of the layers colored in grey. (b) Images of two nanotubes made of 5 and 7 layers, respectively (adapted from Ref. [8]).

image will still consist of fringes but with a different spacing. The cylindrical symmetry of the layers has also been verified from electron energy loss spectroscopy measurements performed by scanning a nanometre probe across a section of the nanotube [15,16].

The image of an individual single-wall nanotube consists of two sets of Fresnel fringes due to the edge-on part of the tube. According to image simulations [11], these fringes are composed of a strong dark fringe bordered by a white fringe followed by very weak fringes. The appearance (thickness and relative position of the dark fringe with respect to the edge-on part of the tube) is very sensitive to the observation conditions which may influence the determination of the tube diameter [11,17].

In contrast to multiwall nanotubes which are very straight, ropes of single wall nanotubes are very flexible and can be easily curved: at low magnification they form

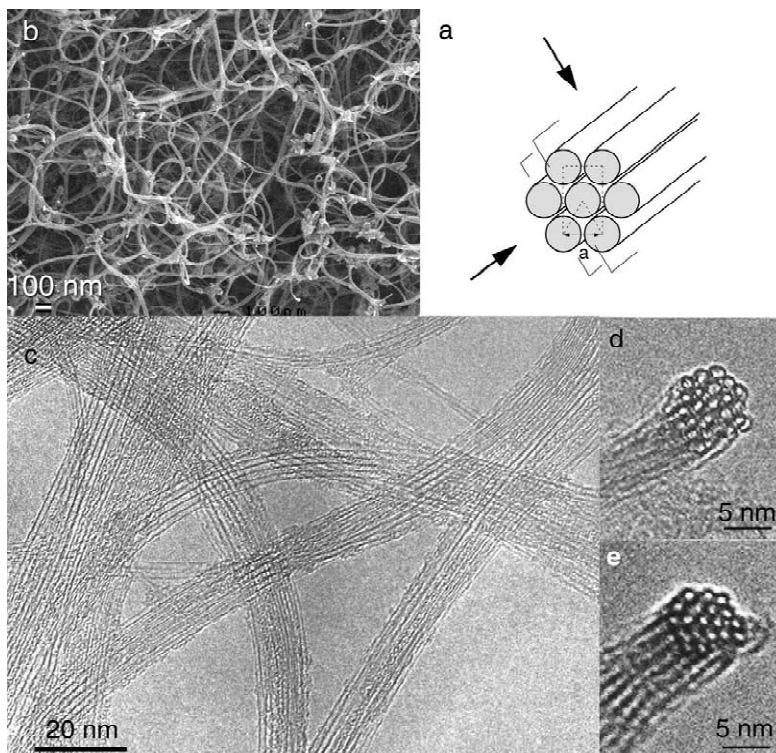


Fig. 2. High resolution TEM analysis of an SWNT rope. (a) Scheme of the structure of the rope and of a family of lattice planes of the tube array. The arrows indicate the two possible directions of observation. (b) Field emission gun scanning electron microscope image of an ensemble of ropes (micrograph L. Vaccarini, Université de Montpellier). (c) Image of several ropes projected perpendicularly to their axis. (d, e) Images of a rope projected along its axis; the focus is close to the Scherzer focus ( $-90$  nm for the Jeol 4000FX microscope) in (d) and twice this value in (e).

complex entangled features reminiscent of a spaghetti plate or wad of hairs (Fig. 2b). Because of this ability to be curved, ropes can be observed in a projection either perpendicular (Fig. 2c) or parallel to their axis (Fig. 2d and e). This later projection condition is particularly interesting since it provides an image of a cross section-like view of the rope and of the single wall tubes building it. In Fig. 2d and e, the images consist indeed of periodic arrays of dark circles having a white dot in their center. Each dark circle is the image of the atomic layer of an SWNT projected along its axis: the observation of the number of SWNT and of the periodicity of their arrangement within the rope is immediate. Nevertheless the determination of the diameter of the SWNT from these images is much more delicate. Careful inspection of Fig. 2d and e reveals differences in the diameter and in the thickness of the dark circles. Image simulations calculated using the EMS software have shown that the appearance of the dark circles is indeed very sensitive to the defocus and orientation conditions [11]. The diameter of the circles is highly focus-dependent and coincides with that of the SWNT for foci close to the Scherzer focus only. This later condition corresponds to the experimental image shown in Fig. 2d. When the focus

is increased from the Scherzer value, the diameter decreases and the thickness of the circle increases. At large focus, the contrast due to the SWNT disappears and the image of a rope consists of an array of white dots located at the center of the SWNTs. This feature is that observed in Fig. 2e.

When the observation of the rope is made perpendicularly to its axis (Fig. 2c), the image is a set of periodic alternating dark and white fringes which correspond to the lattice planes of the tube array parallel to the direction of propagation of the electron beam. Each lattice plane is made of a row of SWNTs (Fig. 2a). The observation of the fringes is therefore the signature that within a rope the SWNTs are periodically packed and that their diameters are very close to each other. If this is not the case one would observe instead of this clear fringe contrast a confused image made of the superimposed images of the individual tubes. According to image simulations [11], the dark fringes may be located at the center of the row of tubes or in between, depending on the defocus. The lattice parameter can be determined from the periodicity of the fringes as this is equal to the lattice planes spacing. For instance, (11) and (20) planes have a spacing equal to

$\sqrt{3}a/2$  and  $a/2$ , respectively, where  $a$  is the lattice parameter. The fringe spacing observed on the images is then directly related to the relative orientation of the rope lattice with respect to the electron beam. An attentive observation of Fig. 2b reveals indeed that the fringe periodicity varies from rope to rope and that it can vary along a given rope. This feature is commonly observed and is due to the fact that the ropes are frequently twisted around their axis. The twist induces a continuous rotation of the lattice planes so that the planes parallel to the electron beam follow a discrete and well-defined sequence—(11), (31), (20), (31), (11) . . .—which corresponds to the sequence of fringe spacings one can observe on the images [18]. Finally the lattice parameter, which can be deduced from the measurement of the periodicity of the fringes, is equal up to a constant (equal to the inter-tube distance) to the mean diameter of the tubes contained in a rope.

## 2.2. Helicities of the nanotubes

Imaging the helicities of the nanotubes requires to be able to image directly the atomic positions. The first direct images have been obtained by imaging the atomic surface of nanotubes using an STM microscope [19]. This method is however restricted to individual single layer nanotubes and does not allow the analysis of a large number of objects. Usual TEM images such as those presented in Figs. 1 and 2 do not provide any information on the helicities of the nanotubes. To do this, it is necessary to obtain direct images of the atomic positions of each tube of the structure and one has to overcome two kinds of difficulties. Firstly, the microscope should have a spatial resolution better than 0.2 nm to be able to separate atoms of first neighbor pairs. Such a resolution is achieved for a few microscopes only. Secondly, the unavoidable observation in projection makes difficult the identification of the atomic positions of several self-assembled layers. An elegant solution to this imaging problem has been brought by examining the signal issued from the nanotube in the Fourier space of the image, which is nothing other than the electron diffraction pattern of the nanotube. This method, detailed in Section 3, has proved its efficiency for analyzing both multiwall nanotubes [20,21] and ropes of SWNTs [22].

The diffraction method becomes inadequate for objects containing a reduced number of layers since the diffracted peaks are very weak and hardly detected. In that case, the only issue is to obtain very high resolution images. This situation has been encountered for BN SWNTs which have been recently synthesized [23]. These nanotubes have an atomic structure similar to that of their carbon analogs, allowing to replace C–C bonds by B–N bonds. Fig. 3a presents the image of a rope of three single layer tubes issued from a nanoparticle of boron, obtained with the Jeol 4000EX microscope (point resolution=0.16 nm). The

nanotube inside the frame shown in Fig. 3a exhibits a dot contrast which is enlarged in Fig. 3b. This dot contrast is only observable on the wall closest to the bottom of the image, the other wall being screened by the adjacent tube. It consists of a periodic sequence of dark lobes at the tube image edge, which are elongated perpendicularly to the tube axis, this periodic array being bordered by two white lines. The periodicity of these dark lobes is 0.21 nm and corresponds to the periodicity of the (10–10) planes of hexagonal BN. Image simulations have been performed with the EMS code for different tube configurations and are presented in Fig. 3c–f. They show that only zig-zag BN-SWNTs exhibit a lobe sequence readily comparable to the experimental images (Fig. 3e). Moreover, these simulations have also shown that regardless of defocus conditions and their corresponding contrast inversions, the black spots lining the walls of the tubes remain a permanent signature of zig-zag BN-SWNTs (Fig. 3f). Thus, these dark spots are ideal for determining whether BN-SWNTs are zig-zag or not. This is a particularly important point to emphasize since these dark dots at the edges are easy to observe in contrast to the full contrast of the BN-SWNT. In fact this last contrast is made of an array of white and black dots which directly reveals the atomic configuration of the BN-SWNTs since they are located at the center of the hexagons of the BN tiling. Unfortunately this dot contrast is very weak and highly sensitive to the orientation of the tubes and to defocus conditions as it can be seen from Fig. 3f. It has been recorded recently for carbon SWNTs thanks to the use of a field emission gun microscope of the latest generation which provides a more coherent and more intense electron beam than classical electron sources [24]. Finally it is worth noticing that TEM images with atomic resolution have also been obtained from carbon MWNTs where the majority of the layers were armchair [25].

## 3. Diffraction

### 3.1. The kinematical theory

In the kinematical theory of diffraction applied to a plane wave with initial wave vector  $\vec{K}_i$ , the total amplitude of the wave diffracted in the direction defined by the scattered wave vector  $\vec{K}_s$  is proportional to the structure factor

$$S(\vec{q}) = \sum_j f_j(q) e^{i\vec{q} \cdot \vec{r}_j} \quad (1)$$

where  $\vec{q} = \vec{K}_i - \vec{K}_s$  is the scattering wave vector, with modulus  $q = 2K_i \sin \theta$  where  $2\theta$  is the scattering angle. The above equation is a coherent sum of atomic factors  $f_j(q)$  multiplied by phase factors depending on the atomic positions  $\vec{r}_j$ . The structure factor  $S(\vec{q})$  of a perfect single-wall nanotube can be obtained in a closed analytical

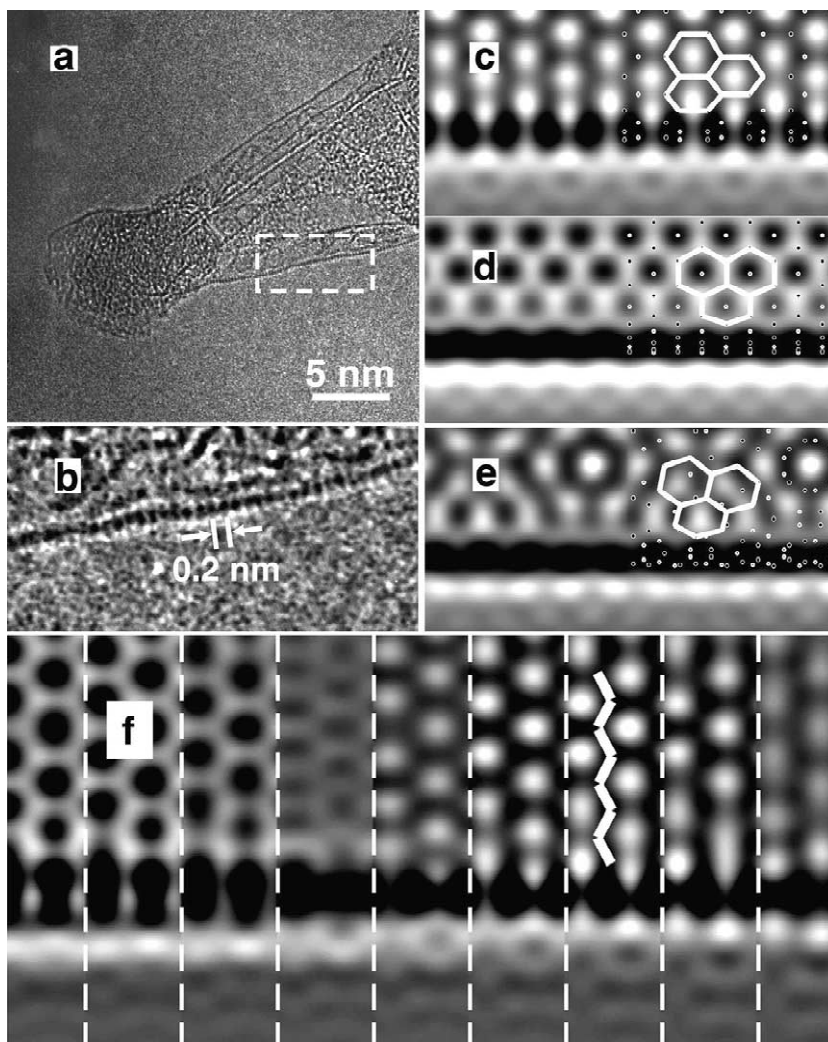


Fig. 3. Helicity analysis of BN-SWNTs. (a) HRTEM of BN-SWNTs emerging from a boron nanoparticle. The exterior wall of the nanotube at the bottom of the image (area within the frame) exhibits a dotted contrast which are a signature of zig-zag BN-NTs; the interior wall is screened by the adjacent BN-NTs. (b) Magnification of the area in the frame in (a). (c, d, e) Simulated images of BN-SWNT, respectively zig zag (configuration (20,0)), armchair (configuration (12,12)) and chiral (configuration (8,16)) calculated using the EMS software with appropriate parameters to simulate the imaging conditions using a JEOL 4000EX (400 kV, Cs=1 mm, focus spread=8 nm, divergence angle=0.7 mrd); the focus is close to the Scherzer focus (-55 nm). The simulated images display along the tube wall (or edge) dark lobes due to the (1010) planes, similar to the those in (A) and (B). B (N) atoms are indicated by small white (dark) dots whereas the positions of the B-N bonds are indicated by tick marks in the image. The 'interior' of the tube exhibits a periodic array of either black or white dots, which are located at the center of the BN hexagons. (f) Focus series of nine simulated images of zig-zag BN-SWNT (configuration (20,0)), the focus varying from -40 nm to -80 nm by 5 nm step (from the left to the right). The contrast of the dot array of the 'interior of the tube' is very weak and highly sensitive to defocus conditions.

expression [26]. For multiwall nanotubes and for ropes of SWNTs, one simply has to add the structure factors of the individual layers.

For X-rays, the atomic factor is related to the electron density. It is of the order of  $Zr_e$ , with  $Z$  the atomic number and  $r_e$  the classical radius of the electron ( $2.8 \times 10^{-15}$  m). With neutrons, the atomic factor of carbon is the coherent diffusion length, also of the order of  $10^{-15}$  m. With

electrons, the atomic factor depends on the screened Coulomb potential of the atom and the length scale here is the Bohr radius ( $5 \times 10^{-11}$  m). As a result, the scattering power of the C atom for electrons is a factor of  $10^8$  larger than for X-rays and neutrons. This explains why electron diffraction can be performed with a single nanotube whereas neutrons and X-rays require a macroscopic quantity. Still, the kinematical theory can be applied to electron

diffraction as long as it remains dominated by single-scattering events. This is the case with carbon nanotubes when the number of layers crossed by the electrons does not exceed a few tens.

### 3.2. Electron diffraction

The atomic structure of individual carbon nanotubes has mostly been investigated by selected-area diffraction in a TEM [8]. Nanodiffraction has been used too, but almost exclusively for the study of ropes of SWNTs [27].

In the electron diffraction pattern of a nanotube [28], the intensities are localized along lines perpendicular to the nanotube axis. Along each line, the intensity is modulated. This modulation is due to the finite width (the diameter) of the nanotube, in close analogy with the oscillations in the diffraction figure of a slit. For a single-wall chiral nanotube, 12 spots with larger intensities are distributed around the vertices of two hexagons inscribed in the first diffraction circle. These hexagons are represented in a computer-generated diffraction pattern of the chiral nanotube (17,4) shown in the central part of Fig. 4. The spots around the first diffraction circle come from the (100) nodes generated by the honeycomb structure. Outside, there is another circle formed by the (110) spots. All the graphene reflections of the type  $(hk0)$  are elongated in the direction normal to the tube axis. Their streaked shape is due to the continuous shortening of the apparent lattice parameter seen by the electrons in the direction normal to the axis when moving from the center to the edges of the tube. The spots are the traces in the Ewald plane of the disks that form the reciprocal space of the nanotube [20].

The splitting of the (100) spots on two hexagons originates from the two halves of the nanotube located on

both sides of the plane through the axis perpendicular to the electron beam (the electron beam is assumed to be perpendicular to the axis). The projection in this plane of the atomic structure of the two nanotube halves are rotated from each other by twice the chiral angle. The diffraction patterns they produce are rotated by the same angle, which means that the angular separation between the two hexagons in the first diffraction circle is two times the chiral angle of the nanotube. The helicity of the atomic structure of a nanotube can therefore be measured directly in the diffraction pattern [8,29], as illustrated in Fig. 4. When the electron beam is not perpendicular to the tube axis, a correction must be applied to the observed angular splitting of the (100) spots [30]. For non-chiral nanotubes, either zig-zag or armchair, the two hexagons in the first diffraction circle coincide (see Fig. 4).

Most of the experimental studies of individual nanotubes by electron diffraction have been realized on multiwall systems. On rare occasions, *isolated* SWNTs have been investigated by this technique [31]. This is because, when by chance an SWNT is isolated, it produces little intensities. The diffraction pattern of an MWNT is close to a superimposition of the patterns produced by the individual layers. In principle, the amplitudes of the wave diffracted by the layers add coherently, and not the intensities. But the interferences between the diffracted waves mostly result in a strong modulation of intensity along the equatorial line only, with a period  $2\pi/c_0$  related to the interlayer spacing  $c_0$  [32], generating thereby the graphite-like (002 $l$ ) spots. The (100) spots around the first diffraction circle are distributed according to the different helicities. From this distribution, it appears that the MWNTs are in general polychiral [8,25]. Most often the number of chiral angles determined from the diffraction

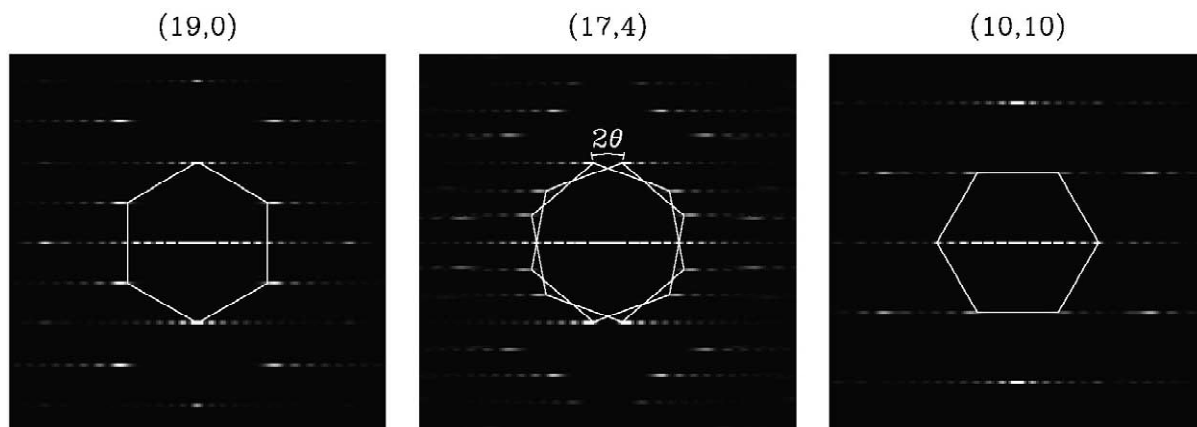


Fig. 4. Computer-generated electron diffraction patterns of three single-wall nanotubes, from left to right: (19,0), (17,4), and (10,10). Their respective chiral angles  $\theta$  are 0, 10.3, and 30°. In each case, the nanotube axis is along the vertical direction, and the electron beam is normal to the axis, perpendicular to the plane of the drawing.

pattern is smaller than the number of walls, which indicates that a few, most likely successive layers adopt the same helicity [33,34]. Now, the actual sequence of chiralities across the layers of an MWNT cannot be determined by diffraction. The reason is that not only the actual sequence influences—weakly—the spot intensities, but also the translation and rotation degrees of freedom of each layer. This represents too many parameters to be determined. Nevertheless, tilting experiments and dark-field contrast imaging may provide some information on the distribution of chiral angles among the layers [35].

Concerning the ropes of SWNTs, early electron nanodiffraction investigations provided the first indication that they were not all made with the same nanotubes [27]. Further nanodiffraction experiments across the ropes did not reveal predominant helicities either, except for occasional observations of preferred armchair configuration [36,37]. Conventional electron diffraction in selected areas of individual ropes confirmed these results [38]. The diffraction pattern of a rope is built from a coherent sum of the structure factors of the constituent nanotubes. The equatorial line of the diffraction pattern now looks spotty since it is modulated by the rapidly-varying phase factors set up by the two-dimensional packing of nanotubes [26]. By contrast, the discrete structure of the (100) and (110) reflections around the first two diffraction circles is washed out, even for well-ordered and untwisted ropes. This observation indicates that the nanotubes in a rope have different chiralities. For a rope composed of nanotubes with chiral angles selected randomly between 0 and 30°, calculations indeed indicate that the highest intensities of the (100) reflections are concentrated in diffuse arcs extending  $\sim 40^\circ$  on both sides of the north and south poles on the first diffraction circle, in agreement with experiment [22]. In contrast to these observations, *small* bundles of SWNTs produced by catalytic chemical vapor deposition may present a unique helicity, as shown recently by selected area electron diffraction [39].

### 3.3. X-ray and neutron diffraction

With X-rays and neutrons, many nanotubes are probed with, in general, all possible orientations with respect to the incident direction. This means that powder-like diffraction profiles are obtained, where the intensity is recorded versus the modulus of the scattering wave vector  $q$  or, equivalently, the scattering angle  $2\theta$ . The nanotubes in the sample have different diameters and chiralities, and they may have different number of layers. As a result of these variations, only a statistical characterization of the sample can be obtained.

For multiwall nanotubes, a diffraction profile is composed of two families of peaks. The graphite-like (002 $l$ ) peaks occur at integer multiples of  $2\pi/c_0$ . Their positions give information on the spacing  $c_0$  between the layers, which is systematically found larger than in HOPG and

close to the value observed in turbostratic graphite [32,40]. These peaks are nearly symmetric in shape. The slight asymmetry is caused by a continuous decrease of the interlayer distance with increasing diameter of the shells [41], the dispersity of the inner diameters, and also to the possible presence of scrolls in the sample [42]. The intensity and width of these peaks depend on the number of layers, on the variations of the interlayer distances, and on lattice distortions [43,44]. The second family of peaks is due to the honeycomb structure of the individual layer and comprises the ( $hk0$ ) reflections of a graphene sheet. These peaks are asymmetric in shape, with a sharp edge on the small- $q$  side, and a tail on the opposite side [40,43]. This shape is a manifestation of the streaking effect induced by curvature, as discussed here above.

Neutrons have the advantage over X-rays that the atomic factor  $f(q)$  does not decrease with  $q$ . A diffraction profile can therefore be obtained up to large values of the wave-vector transfer  $q$ . It contains many Bragg reflections which may reveal much more structural information than X-rays [44]. In particular, the radial distribution function of the nanotubes can be extracted from the neutron diffraction data and compared to that of graphite.

X-ray [43] and neutron [44] diffraction profiles of MWNTs often present additional peaks with smaller intensities than those described above. These peaks correspond to ( $hkl$ ) reflections of graphite which may only exist if some regular stacking of the layers occurs. Short-range interlayer correlation is impossible with perfect cylindrical layers [43]. The presence of these reflections, often seen as weak features in electron diffraction patterns as well [34,45], can be explained by the existence of flat graphitic layers in polygonized tubes [46], or in residual polyhedral carbon particles.

The crystallinity of SWNT ropes can be controlled by examining the Bragg reflections produced by the two-dimensional triangular lattice [47,48]. The most intense peak is the (10) reflection, usually located at about  $q = 0.45 \text{ \AA}^{-1}$  (see Fig. 5). For such small wave vectors, the atomic structure of the nanotubes plays little role and the tubes can be treated as continuous cylinders. The form factor of a cylinder of radius  $r$  is proportional to  $rJ_0(q_\perp r)$  where  $q_\perp$  is the component of the wave vector normal to the tube axis and  $J_0$  is the zeroth order Bessel function. This expression plays the role of  $f(q)$  in Eq. (1). In the theoretical simulation of the powder diffraction profile of the ropes, all the orientations of the nanotube axis must be considered, which can be treated analytically [49]. In addition, both the tube radius  $r$  and the triangular lattice parameter can be treated as adjustable parameters. In an ensemble of ropes, there can be variations of the tube diameters from one rope to the other, or even within the same rope [50], and this dispersity influences the position and shape of the (10) Bragg peak in the average spectrum [51]. Thus, a careful analysis of the diffraction profile between 0 and  $1.8 \text{ \AA}^{-1}$  not only provides the mean value

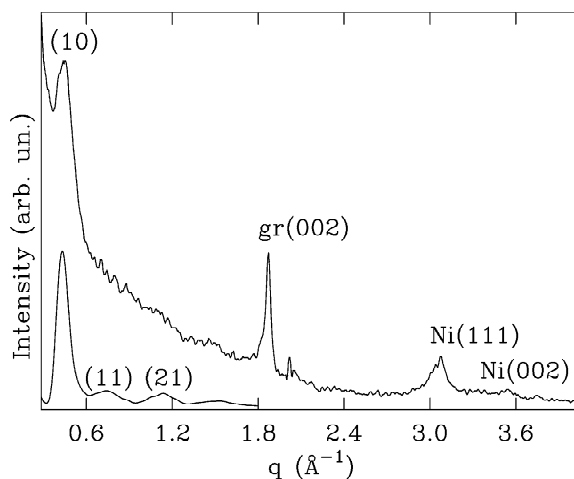


Fig. 5. Top curve, experimental X-ray powder diffraction profile of a sample of SWNT ropes produced by the arc-discharge technique (Ni/Y/C 0.5–0.5–99 at.%). The pattern was acquired at ambient temperature and atmosphere on a computer-controlled Philips 1710 diffractometer equipped with a PW3710 mpd control unit, using a monochromator, Cu K $\alpha$  radiation (tube operated at 40 kV, 30 mA) and a scintillator counter. The data were collected over an angular range from 4° to 60° 2 $\theta$  in continuous scan mode using a scan speed of 0.02° 2 $\theta$ /s. Bottom curve, theoretical diffraction profile computed for an ensemble of ropes with average nanotube diameter 1.34 nm and average number of tubes 25 (see text).

of the tube diameter but also makes it possible to estimate the dispersion of the diameter distribution [49].

As an illustration, the upper curve in Fig. 5 is an experimental X-ray diffraction profile of a C nanotube sample extracted from the collaret in an arc-discharge chamber [48]. The profile presents a clear (10) Bragg peak at 0.43 Å<sup>-1</sup> that indicates the presence of the SWNT ropes. The peak around 1.85 Å<sup>-1</sup> is due to multilayered graphite nanoparticles, probably filled with Ni catalyst whose signature is revealed by two Bragg peaks at 3.1 and 3.5 Å<sup>-1</sup>. The curve at the bottom of Fig. 5 is a theoretical diffraction profile obtained in the continuum limit, as explained above. It was computed for an ensemble of ropes [49], by assuming a Gaussian distribution of nanotube diameters centred at 1.34 nm with root-mean square deviation  $\sigma = 0.13$  nm. The number of tubes in a rope was also treated as a Gaussian variable, with average value 25 and deviation  $\sigma = 5$ . These parameters were adjusted to the experimental diffraction profile. From such adjustment, a global characterization of the ropes is obtained, making it possible to detect the effects of the synthesis conditions and catalyst composition on the mean nanotube diameter [51,52], or to control the efficiency of a purification process [53].

## 4. Scanning probe microscopies

### 4.1. Scanning tunneling microscopy

The first STM investigations of carbon nanotubes revealing their three-dimensional shape were realized on multiwall tubes in 1993 [54,55]. It readily appeared that STM is an ideal tool for a local characterization of the electronic and atomic structures of the nanotubes [56]. With this technique, the nanotubes must be deposited on a homogeneous, flat conducting substrate such as HOPG or Au. Nowadays, the atomic structure of isolated single-wall nanotubes can be resolved more or less routinely with the STM [19,57,58]. Atomic resolution has also been obtained for SWNTs on the top of a rope [50,59]. In principle, both the diameter and chiral angle can be determined from the topographical STM image and, from these two quantities, the wrapping indices  $n$  and  $m$  of the nanotube can be determined. Several effects make this determination difficult.

With a blunt tip, no atomic resolution can be achieved and only a geometrical characterization of the nanotubes is obtained [60,61]. Due to tip-tube convolution effect, a topographic line scan across the nanotube defines a cross-sectional profile whose width  $D$  is larger than the tube diameter  $d_t$  [62]. It is related to the apparent height  $h$  of the tube by the approximate relation  $D = \sqrt{8Rh}$ , where  $R$  is the curvature radius of the tip [63]. The height of the topographic profile  $h$  is close to the diameter of the tube, and  $h$  is often used as a measure of  $d_t$ . But the apparent height depends on the adsorption distance of the nanotube above the substrate and on the difference between the tunneling distances above the tube and over the substrate arising from their different electronic properties. All these distances are not known with precision. Using the apparent height  $h$  of the nanotube seems to *underestimate* the actual diameter by as much as 0.2–0.5 nm [64], perhaps due to the radial compression of the nanotube exerted by the tip.

Atomic resolution can be achieved when the STM tip presents a nanoprotusion that terminates with a single atom. Only the topmost part of the nanotube can be imaged. As an example, Fig. 6 is an experimental image showing two single-wall nanotubes with slightly different chiralities. One clearly sees the triangular lattice formed by the centers of the honeycomb hexagons which appear dark in the image. The diameter can hardly be determined from such an image, except by a suitable fitting procedure of the tunneling current [65]. The atomic corrugation and the cylindrical shape of the first nanotube is revealed by the topographic profile measured along a line perpendicular to the tube, shown in the right-hand side of Fig. 6.

Fig. 7 is a computer simulation of STM images with atomic resolution of three single-wall, metallic nanotubes. These images were computed with a tight-binding Hamiltonian for the case of a point-like tip [66]. In the

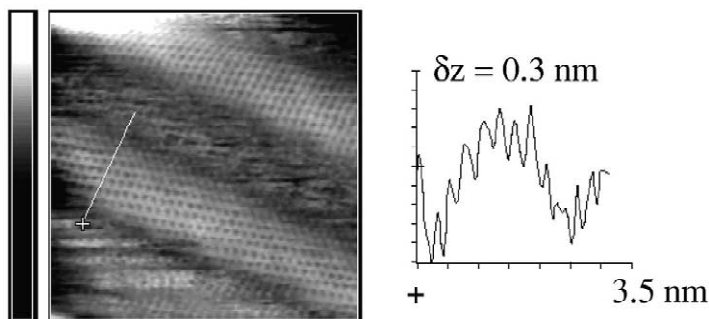


Fig. 6. Atomic resolution STM image of two single wall nanotubes on HOPG. The scan area is  $7.9 \times 7.8$  nm, the grey scale on the left of the image corresponds to 1.3 nm. The sample bias is 0.1 V while the tunneling current is kept at 1 nA. The topographic profile along a line perpendicular to the first nanotube is shown on the right-hand side.

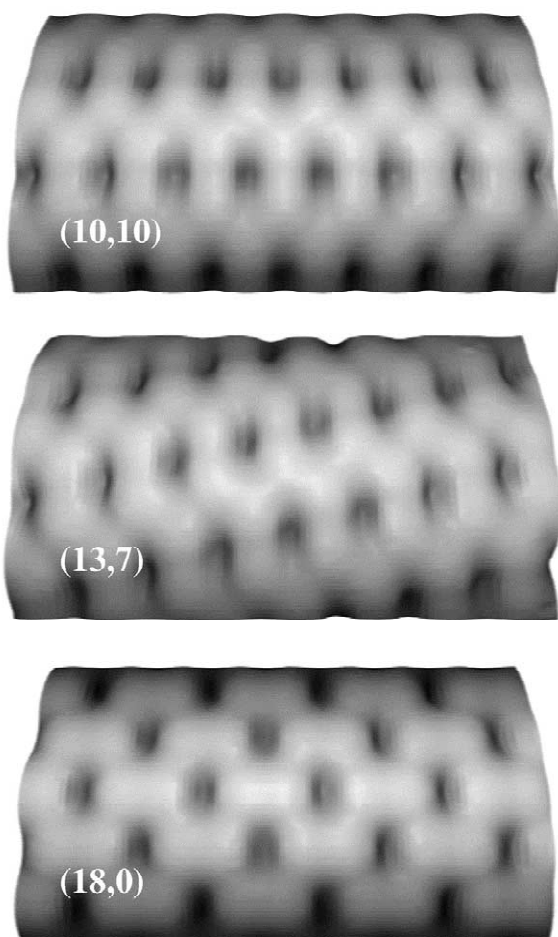


Fig. 7. Computer-generated constant current STM image ( $1.8 \times 1.0$  nm<sup>2</sup>) of three metallic nanotubes computed with a tip potential of 0.2 V.

images, the depressions (dark features) correspond to the centers of the hexagons of the honeycomb structure, where the STM tip gets closer to the nanotube to keep the current constant [66,67]. The prominent features are the C–C bonds. The experiment reveals different kinds of image symmetries [56,68]. The calculations confirm this observation [66,69]. With the armchair geometry (Fig. 7), it is easy to recognize the honeycomb structure in the image since all the bonds look more or less the same [70]. With the zig-zag configuration, there is a strong anisotropy of the bonds [64], the strongest ones are those parallel to the axis and these define a triangular lattice with 0.246 nm parameter. In chiral nanotubes, the anisotropy of the bonds is responsible for the appearance of stripes in the STM image that spiral around the nanotube [56].

In undoped semiconducting nanotubes, the potential applied to the tip must exceed half the band gap. For these nanotubes, the spiral pattern formed by the strongest bonds in the STM image changes its orientation by reversing the applied bias. This effect, clearly illustrated in Fig. 8, was predicted by theory [69] and confirmed by experiment [71]. The bonds that look strongest are those having a bonding character at the energies corresponding to the bias window [72]. The STM current is increased at the center of these bonds by comparison with those with an anti-bonding character. Due to the electron-hole symmetry of the nanotube density of states, this character switches from bonding to anti-bonding or vice versa when crossing the Fermi level.

The chiral angle can be measured in the atomically-resolved image of the nanotube, by measuring the angle between the tube axis and the closest zig-zag direction which is a line joining the hexagon centers separated by the 0.246-nm lattice parameter. In chiral nanotubes, the lines formed by the centers of the hexagons behave similarly like the line (c') in Fig. 9. Therefore, when one tries to take a cross sectional line along such a direction in

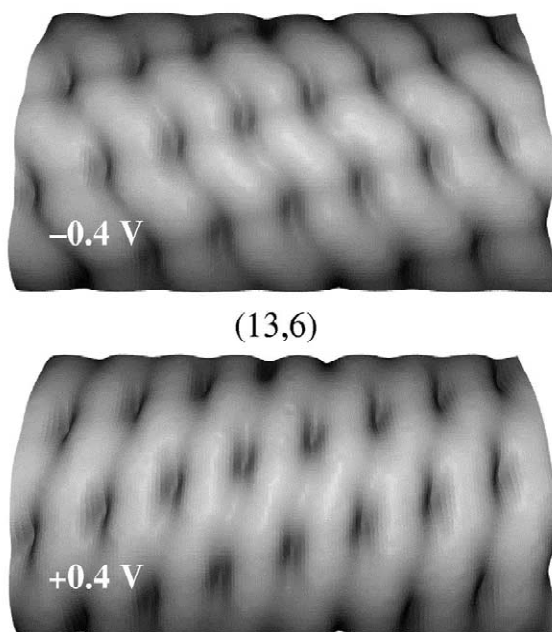


Fig. 8. Computer-generated constant current STM image ( $1.8 \times 1.0 \text{ nm}^2$ ) of the same (13,6) semiconducting nanotube computed with a tip potential of  $-0.4 \text{ V}$  (top) and  $+0.4 \text{ V}$ .

an experimental STM image, it will not be possible to fit rigorously a straight line over the row of dark spots (corresponding to the centers of the hexagons), except when this cross section is taken in the topmost part of the tube and the deviations on the two down-sloping sides of the tube are disregarded. However, in this case, when measuring a nanotube with a small radius, one may have just a few points over which to fit the straight line.

The imaged atomic lattice generally appeared stretched in the direction normal to the nanotube axis [73], and this distorts the measured angles. The largest current density is indeed concentrated along the shortest path between tip and sample, so that the atom that is imaged is not close to the vertical projection of the tip apex but close to normal

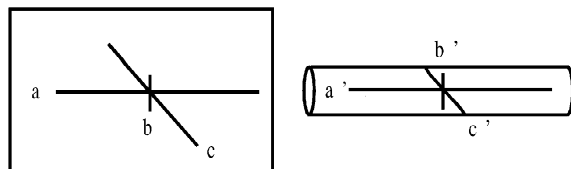


Fig. 9. When folding a rectangle onto a cylinder, the only lines which will appear ‘straight’ as viewed from top—like the STM tip does—will be the lines that are either parallel to the cylinder axis (a; a’) or perpendicular to that direction (b; b’). All other directions will exhibit an ‘S’-like distortion, i.e. the lines will spiral around the cylinder (c; c’).

to the nanotube issued from the tip apex [66]. Due to this geometrical distortion, the angle between the zig-zag and armchair directions in the STM image differs from  $30^\circ$ . By squeezing the image in the transverse direction until restoring the correct  $30^\circ$  between these two directions, the chiral angle can be corrected for the asymmetric distortion [64].

#### 4.2. Scanning tunneling spectroscopy

In scanning tunneling spectroscopy (STS), the variations of the tunneling current  $I$  are traced against the voltage  $V$  applied between tip and sample, for a fixed position of the STM tip. In first approximation, the derivative  $dI/dV$  of the tunneling current is proportional to the electronic density of states of the sample. The first application of that technique to the study of carbon nanotubes was performed in 1994 [74]. When applied to SWNTs, this technique can make a distinction between metallic and semiconducting nanotubes [19,57,58]. In a semiconducting nanotube, the tunneling conductivity is zero in a range of potential whose width corresponds to the band gap. With a metallic tube, the gap is replaced by an interval of constant slope  $dI/dV$  associated with the plateau of density of states around the Fermi level. The width of the band gap  $E_g$  and the metallic plateau  $W$  is easily determined since both of them are delimited by peaks at both ends corresponding to the first Van Hove singularities in the density of states. In first approximation, the separation between these two peaks is inversely proportional to the nanotube diameter and is independent of the chirality [75,76]. For SWNTs with diameter in the nanometre range, the relations to be used for semiconductors and metals are [77]  $E_g = 0.84/d_t$  and  $W = 2.5/d_t$ , respectively, when the energies are in eV and the diameter in nm. In this way, the nanotube diameter can be measured with a reasonable precision [64]. By probing different nanotubes from the same sample with STS, a statistical distribution of diameter can be determined [78].

In addition to giving access to the diameter as explained above, STS may provide information on the actual chirality of the nanotube by comparing the positions of the peaks in the spectrum with the distribution of the Van Hove singularities predicted theoretically [79]. When examined in a large enough interval, the positions of these peaks form a fingerprint of the wrapping indices  $n$  and  $m$  of the nanotube [77]. The technique is not 100% reliable, however, since the electron bands of a nanotube can be modified by the interaction with the substrate [80], especially when a charge transfer takes place [81], and by a radial deformation of the nanotube [82]. Finally, the  $dI/dV$  curve is not an accurate representation of the density of states of the nanotube, since it also depends on the DOS of the STM tip and on the tunneling transmission probability, which is non-symmetric upon reversing the bias voltage [83].

In multiwall nanotubes, the tunneling current probably

probes the last layer. Calculations indeed show that the STM image of a bi-layer nanotube looks very much the same as the one of the external, isolated tube [84]. Another indication is that MWNTs analyzed by STS have been found metallic or semiconducting depending on the diameter and helicity of the outer layer as revealed by STM [85]. However, this interpretation is not fully consistent with Moiré patterns and other superstructures that have occasionally been observed in the STM images of MWNTs, indicating that some interferences exist between the last layers [54]. In addition, the  $I$ - $V$  spectrum may vary a lot along the same nanotube, especially for tubes packed in a bundle [86].

#### 4.3. Atomic force microscopy

With the atomic force microscope (AFM), individual nanotubes and bundles of tubes can be imaged on a scale of tens to hundreds of nanometres [87,88]. Here, the substrate that supports the nanotubes does not need to be conducting.

The diameter of an SWNT can be estimated from the height of the AFM topographic image. As with STM, the width of the topographic profile is more a measure of the tip curvature radius than the diameter of the tube itself due to tip/sample convolution [89]. In the contact mode, this measurement can be distorted by the radial compression of the nanotube produced by the tip [90]. The AFM is more often used in the tapping mode, but even there, the height of the nanotube can be underestimated due to the mechanical response of the nanotube being different from that of the substrate. It is also found frequently that the apparent height of the nanotube examined in tapping-mode AFM oscillates, as a consequence of mechanical vibration of the tube on the substrate [91]. Finally, a nanotube can be deformed by its van der Waals interaction with the substrate, which also affects its apparent height [92].

Recently, atomic resolution has been achieved on individual SWNTs with a scanning force microscope operated with a low-amplitude resonator and equipped with a sharp tip [93]. This is an important issue since the AFM is especially useful for the characterization of nanotubes used in electric transport measurements which require an insulating substrate [94]. With a conducting tip, scanning force and tunneling microscopies can be combined, mak-

ing it possible to see if a nanotube is in electric contact with a lead when inspecting a nanotube-based electronic device [95].

## 5. Optical spectroscopies

### 5.1. Optical absorption spectroscopy

The absorption spectrum of single-wall carbon nanotubes in the near infra-red and visible is generally composed of three peaks corresponding to interband transitions between the first van Hove singularities of the density of states [96–98]. To understand these features, it suffices to realize that the  $i$ th van Hove singularity  $E_{v,i}$  below the Fermi energy  $E_F$  of an SWNT correspond to a local maximum of the  $i$ th valence band along the wave vector axis. For energies close to  $E_F$ , the  $i$ th conduction branch presents a local minimum at the same wave vector where the  $i$ th valence branch has a maximum and this leads to a van Hove singularity  $E_{c,i}$  above the Fermi level. The joint density of states, which corresponds to vertical interband transitions, has sharp peaks at the energies  $E_{i,i} = E_{c,i} - E_{v,i}$  between the  $i$ th van Hove singularities in both the valence band and the conduction band [99]. The corresponding transitions are allowed when the electric field is parallel to the nanotube axis [100]. Their energy ranges are given in Table 1 for nanotubes whose diameters vary between 1.2 and 1.5 nm. The first two peaks in the absorption spectrum are due to the semiconducting nanotubes, the third is due to the metallic tubes [97]. By simply looking at the position and width of the absorption peaks, information is obtained on the diameter distribution of the nanotubes. This is a global technique.

### 5.2. Raman spectroscopy

Raman spectroscopy is a powerful tool for the characterization of single-wall carbon nanotubes [101,102]. A peculiarity of the SWNTs is that the cross section of the Raman scattering is strongly enhanced when the energy of either the incident or scattered photons is in resonance with an electronic transition [101,103]. This effect can be

Table 1  
Resonance conditions in absorption spectroscopy and Raman scattering for a distribution of single-wall carbon nanotubes with diameters  $1.2 < d_t < 1.5$  nm

$\Delta E_{11}^S$	$\Delta E_{22}^S$	$\Delta E_{11}^M$	$\Delta E_{33}^S$
$0.5 < E < 0.7$ eV	$1.0 < E < 1.4$ eV	$1.5 < E < 2.2$ eV	$E > 2.0$ eV

$E_{i,i}^{S,M}$  denotes the vertical interband transition between the  $i$ th van Hove singularities in both the valence and the conduction bands of a semiconducting (S) or metallic (M) nanotube. The transition energies have been computed with the tight-binding Hamiltonian of Ref. [77] ( $\gamma_0 = -2.9$  eV,  $s_0 = 0.13$ ).

exploited to gain information on the electronic structure of the nanotube, and indirectly from that, on the chirality.

An SWNT has 15 or 16 Raman active modes depending on its symmetry. Among these, several *tangential* modes between 1500 and 1600  $\text{cm}^{-1}$  come from the G band of graphite ( $E_{2g}$  C–C stretching vibration at 1582  $\text{cm}^{-1}$ ) that is split by the curvature of the network [104]. At low frequency, the totally symmetric *radial* breathing mode of an SWNT, typically around 180  $\text{cm}^{-1}$ , is also Raman active. For an isolated tube, the frequency of this mode is inversely proportional to the nanotube diameter [101,105]. In a rope of SWNTs, this relation between frequency and inverse diameter is no longer valid. The tube–tube interactions shift the frequency of the radial breathing mode upwards by as much as 8–10% [106–109]. Even when all the nanotubes in the rope are identical, several Raman lines may appear instead of one [110], which complicates the interpretation of the spectrum.

Raman spectroscopy provides global information because the laser beam, of  $\mu\text{m}$  size, probes many ropes. In particular, the low-frequency region of the spectrum is the superposition of the breathing modes of the many constituent nanotubes whose relative intensities are strongly affected by the resonant character of the scattering [101,111]. For this reason, a quantitative analysis of the tube diameter distribution requires detailed spectrum calculations [112]. However, it was shown recently that adsorbing nanotubes on a rough metallic substrate designed for surface-enhanced Raman spectroscopy (SERS) makes it possible to probe a very small number of nanotubes [113,114]. In the best cases, SERS spectra show a single sharp line in the region of the radial breathing mode, which indicates that the few nanotubes probed—possibly a single one—all have the same diameter that can then be estimated from the frequency of the mode [113,115]. The main difficulty for a precise measurement will be to calibrate the frequency–diameter relation that takes into account the role of the substrate.

In Raman spectroscopy, a distinction can be made between metallic and semiconducting nanotubes, since their resonance conditions are different (see Table 1). With a laser operating at 647 nm ( $h\nu = 1.92$  eV) for instance, and assuming a tube diameter distribution between 1.2 and 1.5 nm, the Stokes scattering from the G band ( $E_S = h\nu - 0.2$  eV) is dominated by the metallic nanotubes, whereas the anti-Stokes scattering ( $E_{AS} = h\nu + 0.2$  eV) is nearly out of resonance from the metallic nanotubes [116]. Thanks to this effect, it was possible to attribute a broad Raman line at 1540  $\text{cm}^{-1}$  with asymmetric lineshape to the metallic nanotubes [117]. Like all the tangential components, the frequency of this mode is weakly dependent on nanotube diameter, but the Raman intensity strongly depends on it due to the resonance effect. This property can be exploited to compare the diameter distribution of the nanotubes produced by different techniques or different catalysts [108].

## Acknowledgements

This work was partly funded by the Belgian State Interuniversity Research Program on *Reduced Dimensionality Systems* (PAI/IUAP P4/10). LPB gratefully acknowledges support from the FNRS in Belgium and from OTKA grant T030435 in Hungary. The authors acknowledge Amand Lucas, Luc Henrard, Frederic Moreau, Gezá Márk, Priscilla Simonis, Janos B. Nagy, and Antonio Fonseca for fruitful discussions.

## References

- [1] Ajayan PM. Chem Rev 1999;99:1787–99.
- [2] Hamada N, Sawada SI, Oshiyama A. Phys Rev Lett 1992;68:1579–81.
- [3] Saito R, Fujita M, Dresselhaus G, Dresselhaus MS. Appl Phys Lett 1992;60:2204–6.
- [4] Dekker C. Phys Today 1999;52:22–8.
- [5] Tasaki S, Maekawa K, Yamabe T. Phys Rev B 1998;57:9301–18.
- [6] Hernandez E, Goze C, Bernier P, Rubio A. Phys Rev Lett 1998;80:4502–5.
- [7] Ebbesen TW. Phys Today 1996;49:26–32.
- [8] Iijima S. Nature 1991;354:56–8.
- [9] For a general introduction to HRTEM and its application to the study of carbon structures, see Bernaerts D, Amelinckx S, in: Amelinckx S et al., editors, Handbook of microscopy, vol. 3. New York: VCH, 1996, pp. 437–82.
- [10] Stadelmann P. Ultramicroscopy 1987;21:131–46.
- [11] Journet C. Thèse de doctorat de l'Université de Montpellier II, 1998.
- [12] Bernaerts D. PhD thesis. University of Antwerp, 1997.
- [13] Liu M, Cowley J. Ultramicroscopy 1994;53:333–42; Liu M, Cowley J. Mater Sci Eng A 1994;185:131.
- [14] Amelinckx S, Bernaerts D, Zhang XB, Van Tendeloo G, Van Landuyt J. Science 1995;267:1334–8.
- [15] Stéphan O. Thèse de doctorat de l'Université d'Orsay, 1996.
- [16] Démoncy N, Stéphan O, Brun N, Colliex C, Loiseau A, Pascard H. Eur Phys J B 1998;4:147–57.
- [17] Fan XD, Bursill LA. Phil Mag A 1995;72:139–59.
- [18] Bernier P, Maser W, Journet C, Loiseau A, Lamy de la Chapelle M, Lefrant S et al. Carbon 1998;36:675–80.
- [19] Wildoer JWG, Venema LC, Rinzler AG, Smalley RE, Dekker C. Nature 1998;391:59–62.
- [20] Zhang XB, Zhang XF, Amelinckx S, Van Tendeloo G, Van Landuyt J. Ultramicroscopy 1994;54:237–49.
- [21] Lucas AA, Bruyninckx V, Lambin Ph. Europhys Lett 1996;35:355–60.
- [22] Henrard L, Loiseau A, Journet C, Bernier P. Eur Phys J B 2000;13:661–9.
- [23] Gavillet J, Lamy de la Chapelle M, Cochon JL, Pigache D, Loiseau A. In: Proceedings of EUREM 12, Brno, July, vol. 2, 2000, pp. 261–2; Lee RS, Gavillet J, Lamy de la Chapelle M, Loiseau A, Cochon JL, Pigache D et al. Phys Rev B Rapid Commun, submitted.
- [24] Golberg D, Bando Y, Bourgeois L, Kurashima K. Carbon 1999;37:1858–60;

- Golberg D, Bando Y, Bourgeois L, Kurashima K. *J Appl Phys Lett* 1999;77:1979–81.
- [25] Zhang XF, Zhang XB, Van Tendeloo G, Amelinckx S, Op de Beeck M, Van Landuyt J. *J Cryst Growth* 1993;130:368–82.
- [26] Lambin Ph, Lucas AA. *Phys Rev B* 1997;56:3571–3.
- [27] Cowley JM, Nikolaev P, Thess A, Smalley RE. *Chem Phys Lett* 1997;265:379–84.
- [28] Amelinckx S, Lucas AA, Lambin Ph. *Rep Prog Phys* 1999;62:1471–4.
- [29] Qin LC. *Chem Phys Lett* 1998;297:23–8.
- [30] Zhang XB, Amelinckx S. *Carbon* 1994;32:1537–9.
- [31] Iijima SI, Ichihashi T. *Nature* 1993;363:603–5.
- [32] Saito Y, Yoshikawa T, Bandow S, Tomita M, Hayashi T. *Phys Rev B* 1993;48:1907–9.
- [33] Dravid VP, Lin X, Wang Y, Wang XK, Yee A, Ketterson JB et al. *Science* 1993;259:1601–4.
- [34] Liu M, Cowley JM. *Carbon* 1994;32:393–403.
- [35] Bernaerts D, Op de Beeck M, Amelinckx S, Van Landuyt J, Van Tendeloo G. *Phil Mag A* 1996;74:723–40.
- [36] Qin LC, Iijima S, Kataura H, Maniwa Y, Suzuki S, Achiba Y. *Chem Phys Lett* 1997;268:101–6.
- [37] He RR, Jin HZ, Zhu J, Yan YJ, Chen XH. *Chem Phys Lett* 1998;298:170–6.
- [38] Bernaerts D, Zettl A, Chopra NG, Thess A, Smalley RE. *Solid State Commun* 1998;105:145–9.
- [39] Colomer JF, Henrard L, Lambin PH, Van Fendeloo G. *Phys Rev B* 2001;64:125425–7.
- [40] Zhou O, Fleming RM, Murphy DW, Chen CH, Haddon RC, Ramirez AP et al. *Science* 1994;263:1744–7.
- [41] Kiang CH, Endo M, Ajayan PM, Dresselhaus G, Dresselhaus MS. *Phys Rev Lett* 1998;81:1869–72.
- [42] Bandow S. *Jpn J Appl Phys Part 2* 1997;36:L1403–1405.
- [43] Reznik D, Olk CH, Neumann DA, Copley JRD. *Phys Rev B* 1995;52:116–24.
- [44] Burian A, Dore JC, Fischer HE, Sloan J. *Phys Rev B* 1999;59:1665–8.
- [45] Bernaerts D, Amelinckx S, Lambin Ph, Lucas AA. *Appl Phys A* 1998;66:53–64.
- [46] Amelinckx S, Bernaerts D. In: Yoshimura Y, Chang RPH, editors. *Supercarbon, synthesis, properties and application*, Springer series in materials science, Berlin: Springer, 1998, pp. 51–80.
- [47] Thess A, Lee R, Nikolaev P, Dai H, Petit P, Robert J et al. *Science* 1996;273:483–7.
- [48] Journet C, Maser WK, Bernier P, Loiseau A, Lamy de la Chapelle M, Lefrant S et al. *Nature* 1997;388:756–8.
- [49] Rols S, Almairac R, Henrard L, Anglaret E, Sauvajol JL. *Eur Phys J* 1999;10:263–70.
- [50] Obratsova ED, Yurov VYu, Shevluga VM, Baranovsky RE, Nalimova VA, Kuznetsov VL et al. *Nanostruct Mater* 1999;11:295–306.
- [51] Anglaret E, Rols S, Sauvajol JL. *Phys Rev Lett* 1998;81:4780.
- [52] Bandow S, Asaka S, Saito Y, Rao AM, Grigorian L, Richter E et al. *Phys Rev Lett* 1998;80:3779–82.
- [53] Rinzler AG, Liu J, Dai H, Nikolaev P, Huffman CB, Rodríguez-Macías FJ et al. *Appl Phys A* 1998;67:29–37.
- [54] Ge M, Sattler K. *Science* 1993;260:515–8.
- [55] Zhang Z, Lieber CM. *Appl Phys Lett* 1993;62:2792–4.
- [56] Clauss W. *Appl Phys A* 1999;69:275–81.
- [57] Odom TW, Huang JL, Kim Ph, Lieber ChM. *Nature* 1998;391:62–4.
- [58] Hassanién A, Tokumoto M, Kumazawa Y, Kataura H, Maniwa Y, Suzuki S et al. *Appl Phys Lett* 1998;73:3839–41.
- [59] Clauss W, Bergeron DJ, Johnson AT. *Phys Rev B* 1998;58:R4266–4269.
- [60] Gallagher MJ, Chen D, Jacobsen BP, Sarid D, Lamb LD, Tinker FA et al. *Surf Sci* 1993;281:L335–340.
- [61] Hubler U, Jess P, Lang HP, Güntherodt HJ, Salvétat JP, Forró L. *Carbon* 1998;36:697–700.
- [62] Márk GI, Biró LP, Gyulai J. *Phys Rev B* 1998;58:12645–8.
- [63] Biró LP, Lazarescu S, Lambin Ph, Thiry PA, Fonseca A, Bnagy J et al. *Phys Rev B* 1997;56:12490–8.
- [64] Venema LC, Meunier V, Lambin Ph, Dekker C. *Phys Rev B* 2000;61:2991–6.
- [65] Odom TW, Huang JL, Kim Ph, Ouyang M, Lieber ChM. *J Mater Res* 1998;13:2380–8.
- [66] Meunier V, Lambin Ph. *Phys Rev Lett* 1998;81:5888–91.
- [67] Rubio A, Sanchez-Portal D, Artacho E, Ordejon P, Soler JM. *Phys Rev Lett* 1999;82:3520–3.
- [68] Venema LC, Wildoer JWG, Dekker C, Rinzler AG, Smalley RE. *Appl Phys A* 1998;66:S153–155.
- [69] Kane CL, Mele EJ. *Phys Rev B* 1999;59:R12759–12762.
- [70] Venema LC, Wildoer JWG, Janssen JW, Tans SJ, Temminck Tuinstra HLL, Kouwenhoven LP et al. *Science* 1999;283:52–5.
- [71] Clauss W, Bergeron DJ, Freitag M, Kane CL, Mele EJ, Johnson AT. *Europhys Lett* 1999;47:601–7.
- [72] Meunier V, Senet P, Lambin Ph. *Phys Rev B* 1999;60:7792–5.
- [73] Ge M, Sattler K. *Appl Phys Lett* 1994;65:2284–6.
- [74] Olk CH, Heremans JP. *J Mater Res* 1994;9:259–62.
- [75] Mintmire JW, White CT. *Phys Rev Lett* 1998;81:2506–9.
- [76] Charlier JC, Lambin Ph. *Phys Rev B* 1998;57:R15037–15039.
- [77] Saito R, Dresselhaus G, Dresselhaus MS. *Phys Rev B* 2000;61:2981–90.
- [78] Wirth I, Eisebitt S, Kann G, Eberhardt W. *Phys Rev B* 2000;61:5719–23.
- [79] Kim Ph, Odom TW, Huang J, Lieber CM. *Carbon* 2000;38:1741–4.
- [80] Rubio A. *Appl Phys A* 1999;68:275–82.
- [81] Xue Y, Datta S. *Phys Rev Lett* 1999;83:4844–7.
- [82] Yang L, Han J. *Phys Rev Lett* 2000;85:154–7.
- [83] Márk GI, Biró LP, Gyulai J, Thiry PA, Lucas AA, Lambin Ph. *Phys Rev B* 2000;62:2797–805.
- [84] Lambin Ph, Meunier V, Rubio A. *Phys Rev B* 2000;62:5129–35.
- [85] Hassanién A, Tokumoto M, Ohshima S, Kuriki Y, Ikazaki F, Uchida K et al. *Appl Phys Lett* 1999;75:2755–7.
- [86] Biró LP, Thiry PA, Lambin Ph, Journet C, Bernier P, Lucas AA. *Appl Phys Lett* 1998;73:3680–2.
- [87] Ebbesen TW, Hiura H, Fujita J, Ochiai Y, Matsui S, Tanigaki K. *Chem Phys Lett* 1993;209:83–90.
- [88] Muster J, Duesberg GS, Roth S, Burghard M. *Appl Phys A* 1999;69:261–7.
- [89] Höper R, Workman RK, Chen D, Sarid D, Ydav T, Withers JC et al. *Surf Sci* 1994;311:L731–736.
- [90] Shen W, Jiang B, Han BS, Xie SS. *Phys Rev Lett* 2000;84:3634–7.
- [91] Biró LP, Gyulai J, Márk GI, Daróczy CsS. *Micron* 1999;30:245–54.
- [92] Hertel T, Walkup RE, Avouris Ph. *Phys Rev B* 1998;58:13870–3.

- [93] Clauss W, Zhang J, Bergeron DJ, Johnson AT. *J Vac Sci Technol B* 1999;17:1309–12.
- [94] Tans SJ, Devoret MH, Dai H, Thess A, Smalley RE, Geerligs LJ et al. *Nature* 1997;386:474–7.
- [95] Clauss W, Freitag M, Bergeron DJ, Johnson AT. *Carbon* 2000;38:1735–9.
- [96] Petit P, Mathis C, Journet C, Bernier P. *Chem Phys Lett* 1999;305:370–4.
- [97] Kataura H, Kumazawa Y, Maniwa Y, Umezu I, Suzuki S, Ohtsuka Y et al. *Synth Met* 1999;103:2555–8.
- [98] Jost O, Gorbunov AA, Pompe W, Pichler T, Friedlein R, Knupfer M et al. *Appl Phys Lett* 1999;75:2217–9.
- [99] Lin MF, Shung KWK. *Phys Rev B* 1994;50:17744–7.
- [100] Mintmire JW, White CT. *Synth Met* 1996;77:231–4.
- [101] Rao AM, Richter E, Bandow S, Chase B, Eklund PC, Williams KA et al. *Science* 1997;275:187–91.
- [102] Lamy de la Chapelle M, Lefrant S, Journet C, Maser W, Bernier P, Loiseau A. *Carbon* 1998;36:705–8.
- [103] Richter E, Subbaswamy KR. *Phys Rev Lett* 1997;79:2738–41.
- [104] Kasuya A, Sasaki Y, Saito Y, Tohji K, Nishina Y. *Phys Rev Lett* 1997;78:4434–7.
- [105] Kurti J, Kresse G, Kuzmany H. *Phys Rev B* 1998;58:R8869–8872.
- [106] Venkateswaran UD, Rao AM, Richter E, Menon M, Rinzler A, Smalley RE et al. *Phys Rev B* 1999;59:10928–34.
- [107] Henrard L, Hernandez E, Bernier P, Rubio A. *Phys Rev B* 1999;60:R8521–8524.
- [108] Alvarez L, Righi A, Guillard T, Rols S, Anglaret E, Laplaze D et al. *Chem Phys Lett* 2000;316:186–90.
- [109] Rols S, Righi A, Alvarez L, Anglaret E, Almairac R, Journet C et al. *Eur Phys J B* 2000;18:201–5.
- [110] Henrard L, Lambin Ph, Rubio A. In: Kuzmany H, Fink J, Mehring M, Roth S, editors, *Electronic properties of novel materials—molecular nanostructures*, AIP conference proceedings, vol. 544, New York: American Institute of Physics, 2000, pp. 266–70.
- [111] Kuzmany H, Burger B, Hulman M, Kurti J, Rinzler AG, Smalley RE. *Europhys Lett* 1988;44:518–24.
- [112] Milnera M, Kurti J, Hulman M, Kuzmany H. *Phys Rev Lett* 2000;84:1324–7.
- [113] Duesberg GS, Blau WJ, Byrne HJ, Muster J, Burghard M, Roth S. *Chem Phys Lett* 1999;310:814.
- [114] Lefrant S, Louarn G, Baltog I, Baibarac M, Journet C, Bernier P et al. *Synth Met* 1999;100:13–27.
- [115] Azoulay J, Débarre A, Richard A, Tchénio P, Bandow S, Iijima S. *Chem Phys Lett* 2000;331:347–53.
- [116] Kneipp K, Kneipp H, Corio P, Brown SDM, Shafer K, Motz J et al. *Phys Rev Lett* 2000;84:3470–3.
- [117] Pimenta MA, Marucci A, Empedocles SA, Bawendi MG, Hanlon EB, Rao AM et al. *Phys Rev B* 1998;58:R16016–16019.